International Journal of Heat and Mass Transfer 52 (2009) 271–280

Contents lists available at ScienceDirect

International Journal of Heat and Mass Transfer

journal homepage: www.elsevier.com/locate/ijhmt

Pressure effects on flow boiling instabilities in parallel microchannels

C.-J. Kuo, Y. Peles *

Department of Mechanical, Aerospace and Nuclear Engineering, Rensselaer Polytechnic Institute, Troy, NY 12180, USA

ARTICLE INFO

Article history:
Received 5 November 2007
Received in revised form 22 April 2008
Available online 14 August 2008

Keywords:
Flow instability
Boiling
Microchannel
CHF

ABSTRACT

The effects of pressure on flow boiling instabilities in microchannels were experimentally studied. Experiments were conducted using water in 223 μm hydraulic diameter microchannels with mass fluxes ranging from 86 to 520 kg/m^2 s and pressures ranging from 50 to 205 kPa. Onset of flow oscillation, critical heat flux (CHF) conditions, local transient temperature measurements along with flow boiling visualization were obtained and studied. System pressure was found to significantly affect flow instabilities. For high pressure, it was observed that boiling instabilities were significantly delayed and CHF was extended to high mass qualities. Local temperature measurements also revealed lower magnitudes and higher frequencies of oscillations at high system pressures.

1. Introduction

Flow boiling in microchannel heat sinks has received considerable attention in the last several years [1–5]. One of the major issues hindering the practical realization of this cooling method is flow instabilities and oscillations. Flow oscillations can temporally affect flow rate, pressure drop and surface temperature, trigger premature critical heat flux (CHF) condition, and cause structural failure [6–16]. Developing knowledge about these deleterious phenomena at the micro-scale and the conditions leading to their appearance is an important fundamental task.

From the various instabilities encountered during flow boiling, several modes appear to be important in microchannels: *excursive* (and *parallel channel*) *instability*, *compressible volume/pressure drop instability*, *rapid bubble growth*, and CHF conditions. As discussed by Boure et al. [6], the occurrences of *excursive* and *compressible volume instabilities* are characteristic of the negative slope of the channel demand pressure drop–mass flux (Δp–G) curve for constant heat flux (Fig. 1). If the absolute pressure drop–mass flux curve slope of the pump (e.g., curve A in Fig. 1) is lower than the corresponding channel demanded Δp–G curve (segment f–d in Fig. 1), operating the system between points d and f will trigger *excursive* and *compressible volume instabilities*, resulting in transition to CHF condition. To mitigate the excursive instability, several steps can be taken: installing inlet restrictors that modify the channel pressure drop–mass flux curve to a positive slope for mass flux smaller than point d in Fig. 1; using a pump with a stiff supply curve (e.g., curve B in Fig. 1); and reducing the negative slope of segment d–f.

The *rapid bubble growth instability* is unique to micro-domains. It refers to the process that starts when a spherical bubble grows until it attains a size comparable to the channel hydraulic diameter. The bubble then grows explosively in the longitudinal direction, downstream as well as upstream, causing flow reversal. This flow oscillation is a result of two effects: the high liquid superheated temperature required initiating bubble nucleation, and the elevated pressures generated during the rapid growth of the bubble. The large disturbance caused by this bubble growth can also prematurely trigger *excursive instability* by temporally reducing the mass flux to a value below the corresponding onset of flow instability (OFI) (from c to c′ in Fig. 1).

In an effort to suppress boiling instabilities, several studies suggested to place inlet restrictors at the channels inlet [17–19]. This, however, comes with the penalty of increased pressure drop. Artificial boiling-enhanced cavities on the surface, which promote nucleation of bubbles during boiling [20–22], have been shown to moderate instabilities [23,24]. The system pressure, which has been shown to be an important parameter controlling flow oscillation in conventional scale [6], has not been extensively studied at the micro-scale. In this study, flow boiling experiments were conduct at different exit pressures to study pressure effect on flow boiling instabilities in microchannels.

2. Device overview

The microchannel device consists of five parallel, 10,000 μm long, 200 μm wide, and 250 μm deep microchannels spaced 200 μm apart. The microchannel sidewall encompasses an array of 100 reentrant cavities spaced 100 μm apart (Fig. 2). An acute angle connects the 7.5 μm mouth to each of the 50 μm inside diameter reentrant body. In order to minimize ambient heat loss, an air

* Corresponding author. Tel.: +1 518 276 2886; fax: +1 518 276 2623.
E-mail address: pelesy@rpi.edu (Y. Peles).

0017-9310/$ - see front matter © 2008 Elsevier Ltd. All rights reserved.
doi:10.1016/j.ijheatmasstransfer.2008.06.015

Nomenclature

A_p	platform area (heating surface area above the heater) (m^2)
A_s	channel cross-section area (m^2)
$A_{s,tot}$	total channel cross-section area (m^2)
c_p	specific heat (J/kg K)
D	active nucleation site diameter (m)
D_d	Bubble departure diameter (m)
G	mass flux (kg/m^2 s)
h_{lv}	latent heat of vaporization (J/kg)
h_{sp}	single-phase heat transfer coefficient (W/m^2 °C)
I	electrical current (Å)
k_l	thermal conductivity of the liquid (water) (W/m °C)
k_s	thermal conductivity of the substrate (silicon) (W/m °C)
L	distance from the inlet of the microchannel (m)
L_0	channel length (m)
P	pressure (kPa)
P	electrical power (W)
q''	heat flux (W/cm^2)
q''_{eff}	effective heat flux (W/cm^2)
Q_{loss}	heat loss (W)
R	electrical resistance (Ω)
T	thickness of the silicon substrate (m)
T	temperature (°C)
T_1, T_2, T_3	local surface temperatures (°C)
$\overline{T}_{heater}$	average heater temperature (°C)
T_s	substrate temperature (°C)
T_{sat}	saturation temperature (°C)
$T_{thermistor}$	thermistor temperature (°C)
T_w	channel wall temperature (°C)
$\Delta T_{in,sub}$	liquid inlet subcooled temperature (°C)
ΔT_{sub}	bulk liquid subcooled temperature (°C)
ΔT_w	wall superheat (°C)
V	electrical voltage (V)
x	mass quality

Greek letters

δ_t	thermal boundary layer thickness (m)
ϕ	contact angle (°)
ρ	density (m^3/s)
σ	surface tension (N/m)

Subscripts

eff	effective
e	exit
f	fluid
l	liquid
max	maximum
min	minimum
sat	saturation
sp	single-phase
sub	subcooled
v	vapor

gap is formed on the two ends of the side walls, and an inlet and an exit manifolds are etched on the thin silicon substrate (~200 μm). A pyrex cover seals the device from the top and allows flow visualization. Fig. 3a depicts a schematic model of the backside of the device. Three thermistors, 10 μm wide and 300 μm long (Fig. 3b), are located 3400 μm, 6700 μm, and 10,000 μm downstream the channel inlet together with electrical connecting vias. On top of the thermistors, a 1 μm silicon oxide layer is deposited for electrical insulation. A heater is then formed on top of the oxide layer to deliver the heating power and also serves as an additional thermistor to measure the average temperature of the entire microchannel area.

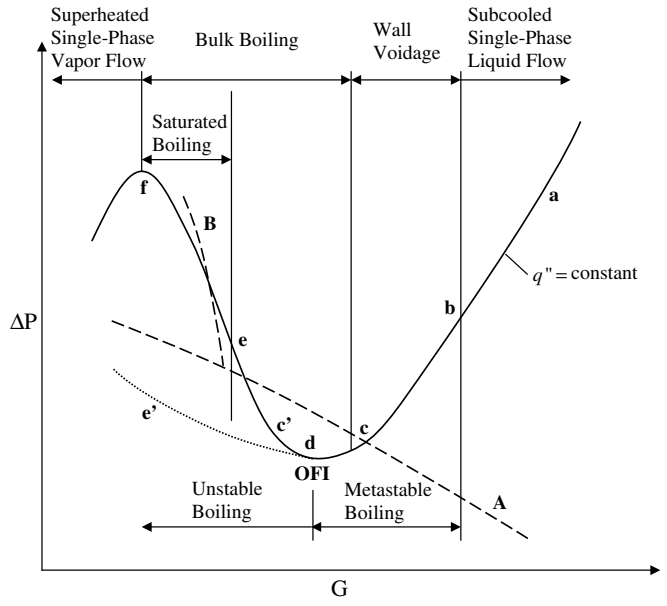

Fig. 1. Mass flux dependence of pressure drop for microchannel and external pump.

3. Device fabrication, experimental apparatus, and procedures

3.1. Microchannel fabrication method

The micro-electro-mechanical system (MEMS) device was micromachined on a polished double-sided n-type ⟨100⟩ single crystal silicon wafer employing techniques adapted from integrated circuit (IC) manufacturing. A 1 μm thick high-quality oxide film was deposited on both sides of the silicon wafer to shield the bare wafer surface during processing and to serve as an electrical insulator. A layer of 150 Å thick titanium was deposited by a CVC 601 sputter deposition system and patterned on the backside of the wafer to form the thermistors. Vias of 0.2 μm aluminum containing 1% silicon and 4% copper was subsequently formed in order to create electrical connections to the thermistors. Following, a 1 μm thick plasma enhanced chemical vapor deposition (PECVD) oxide was deposited to insulate the thermistors and the vias from the lower layer. The heater was then formed on top of the oxide layer by CVC sputtering deposition. A 70 Å thick layer of titanium was initially deposited to enhance adhesion characteristics and was followed by sputtering a 1 μm thick layer of Al–1%Si–4%Cu. Subsequent photolithography and concomitant wet bench processing created the heater on the backside of the wafer. Another 1 μm thick PECVD oxide was deposited to protect the back side features during further processing.

Next, the microchannels were formed on the top side of the wafer. The wafer was taken through a photolithography step and a reactive ion etching (RIE) oxide removal process to mask certain areas on the wafer, which were not to be etched during the deep reactive ion etching (DRIE) process. The wafer was consequently

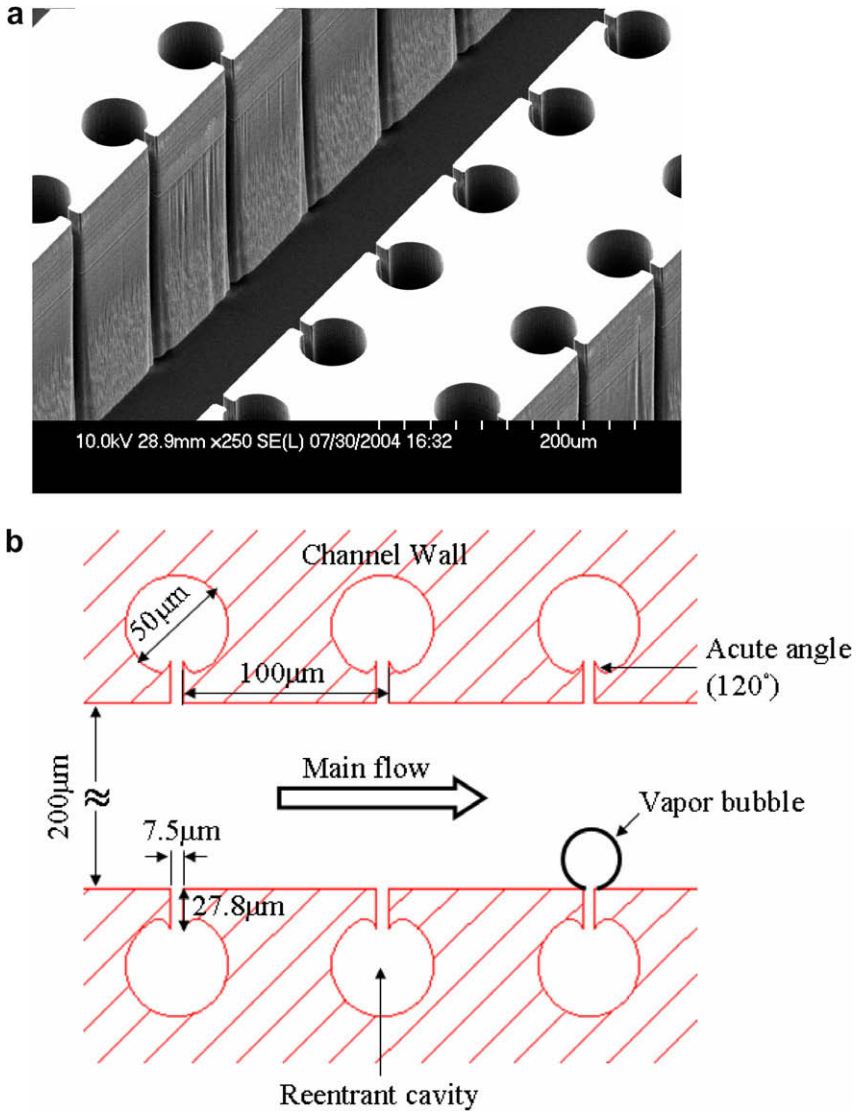

Fig. 2. (a) A SEM image, (b) a CAD model of the microchannel and the reentrant cavities.

etched in the DRIE process, and silicon was removed from places not protected by the photoresist/oxide mask with a characteristic sidewall roughness ~0.3 μm. A profilometer and a scanning electron microscope (SEM) were employed to measure and record various dimensions of the device.

The wafer was flipped, and the backside was then processed to create an inlet, outlet, side air gap, and pressure port taps for the transducers. Photolithography steps followed by a buffered oxide etch (BOE) (6:1) oxide removal process was carried out to create a pattern mask. The wafer was then etched-through in a DRIE process to create the fluidic ports. Thereafter, electrical contacts/pads were opened on the backside of the wafer by performing another round of photolithography and RIE processing. Finally, the processed wafer was stripped of any remaining resist or oxide layers and anodically bonded to a 1 mm thick polished Pyrex (glass) wafer to form a sealed device. After successful completion of the bonding process, the processed stack was die-sawed to separate the devices from the parent wafer.

3.2. Experimental test rig

The setup, shown in Fig. 4, consists of three primary subsystems: the flow loop section, instrumentation, and a data acquisition system. The test section houses the MEMS microchannel devices and its fluidic and thermal packaging module. The microchannel device is mounted on the fluidic packaging module through miniature "o-rings" to ensure a complete leak-free system. The fluidic packaging delivers the working fluid and access to the pressure transducers. The external electrical connections to the thermistors and the heater were achieved from beneath through spring-loaded probe pins, which connected the thermistors and the heater to electrical pads residing away from the main microchannel body.

The main flow loop includes the microchannel device, a pulseless gear pump, a reservoir, which consists of a deaerator unit and a heating element to control the inlet temperature, a flow meter, and a dissolved oxygen meter. The test section heater is connected to a power supply with an adjustable DC current to provide power to the device. The thermistors output signals are recorded by the National Instrument data acquisition system. Simultaneously, the inlet pressure and test section pressure drop are collected, and the boiling process in the microchannels is recorded by a Phantom V4.2 high-speed camera (maximum frame rate of 90,000 frames/s, and 2 μs exposure time) mounted over a Leica DMLM microscope. Calibration of the heater and the thermistors is performed prior to the experiment by placing the device in an oven and establishing the resistance–temperature curve for each individual sensor.

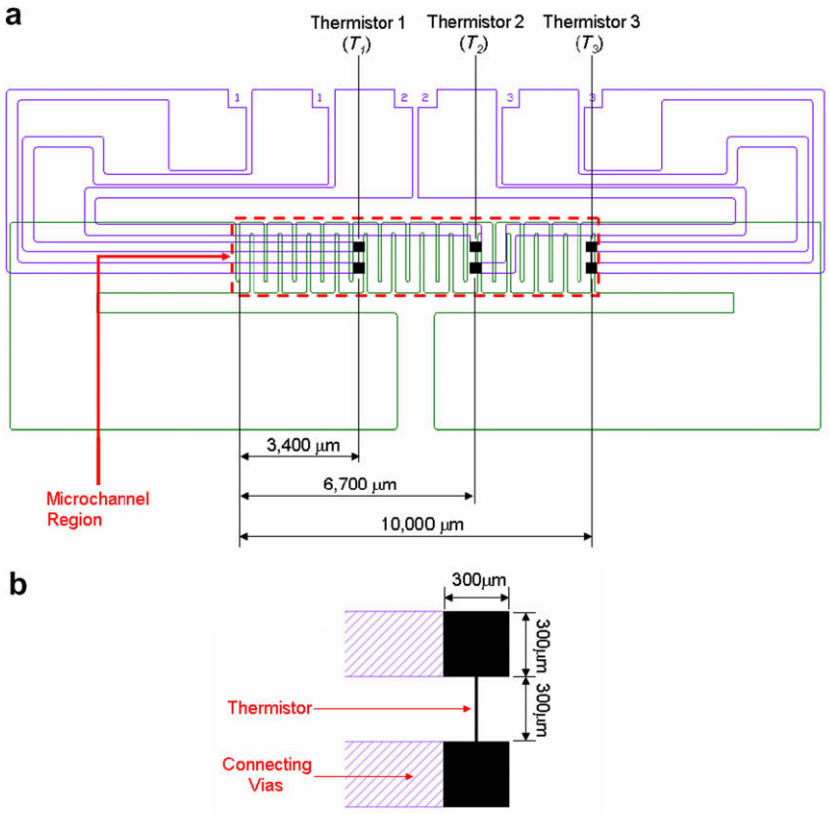

Fig. 3. CAD models of (a) the heater and the thermistors on the back side of the micro-device, (b) a single thermistor.

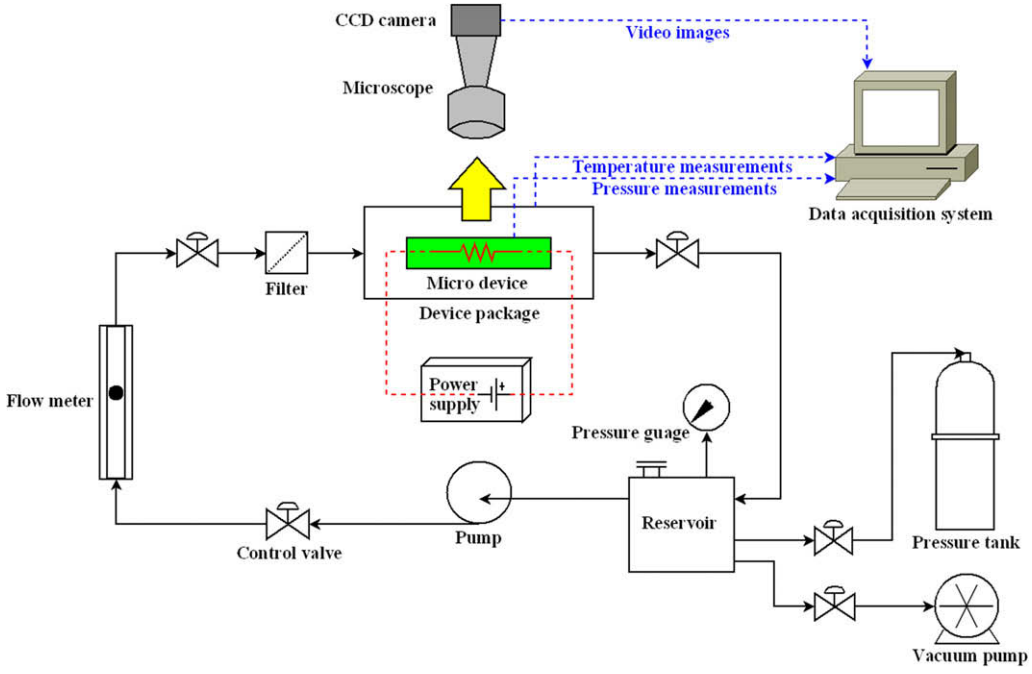

Fig. 4. Experiment setup.

3.3. Experimental procedures and data reduction

The deionized water was first degassed until the oxide concentration level dropped below 3 ppm. Then, the system pressure was set up to a desired value. The water flow rate was fixed, and experiments were conducted after steady conditions were reached with exit pressure and ambient room temperature (~22 °C). The electrical resistances of the thermistors were also measured at room temperature. During the experiment, voltage was applied in 0.5 V increments to the test section heater, and the resistance data for

the heater and the thermistors were recorded once steady state was reached. The procedure was repeated for different flow rates.

To estimate heat losses, electrical power was applied to the test section after evacuating the water from the test loop. Once the temperature of the test section became steady, the temperature difference between the ambient and test section was recorded with the corresponding power. The plot of power versus temperature difference was used to calculate the heat loss ($\dot{Q}_{loss}$) associated with each experimental data point.

Data obtained from the voltage, current, and pressure measurements were used to calculate the surface temperatures, heat flux, and CHF conditions. The electrical input power, P, and heater resistance, R, respectively, were determined by the measured voltage, V, and current, I, with:

$$P = V \times I \tag{1}$$

and

$$R = V/I \tag{2}$$

The electrical resistance–temperature calibration curve of the heater and the thermistors were used for determining the average heater temperature, $\overline{T}_{heater}$, and the thermistor temperature for each local position, $T_{thermistor}$. The substrate temperature, T_s, and the local surface temperatures (T_1, T_2, T_3) at the base of the microchannels were then calculated as:

$$T_s = \overline{T}_{heater} - \frac{(P - \dot{Q}_{loss})t}{k_s A_p} \tag{3}$$

$$T_1, T_2, T_3 = T_{thermistor} - \frac{(P - \dot{Q}_{loss})t}{k_s A_p} \tag{4}$$

where t, k_s, and A_p, are the substrate thickness, thermal conductivity of silicon, and the platform area, respectively. The effective heat flux, q''_{eff}, was defined as:

$$q''_{eff} = \frac{P - \dot{Q}_{loss}}{A_p} \tag{5}$$

The local mass quality at a distance L from the inlet was obtained by:

$$x = \frac{(P - \dot{Q}_{loss})(L/L_0) - GA_{s,tot}c_p\Delta T_{in,sub}}{GA_{s,tot}h_{lv}} \tag{6}$$

where L_0, G, $\Delta T_{in,sub}$, and $A_{s,tot}$ are the total channel length, mass flux, liquid inlet subcooled temperature, and the total channel cross-section area ($A_{s,tot} = 5A_s$ for the current device), respectively.

The uncertainties of the measured values are obtained from the manufacturers' specification sheets, while the uncertainties of the derived parameters are calculated using the method developed by Kline and McClintock [25]. Uncertainty in the mass flux (G), heat flux (q''), temperature (T), and mass quality (x) are estimated to be ±2%, ±1%, ±1%, and ±3%, respectively.

4. Results and discussion

4.1. Boiling trend and the effect of system pressure

Fig. 5 shows the substrate temperature, T_s, as a function of the effective heat flux for exit pressures 50 kPa, 101 kPa, and 205 kPa and mass flux ranging from 86 kg/m^2 s to 520 kg/m^2 s. For all pressures, single-phase liquid flow existed at low heat fluxes followed by onset of nucleate boiling (ONB), and at a certain threshold heat flux, the CHF condition was triggered in which a small increase of heat flux resulted in an abrupt rise of the substrate temperature. ONB was evident by a radical change in the q''_{eff}–T_s slope. Flow visualization of vapor bubble forming on the channel wall confirmed

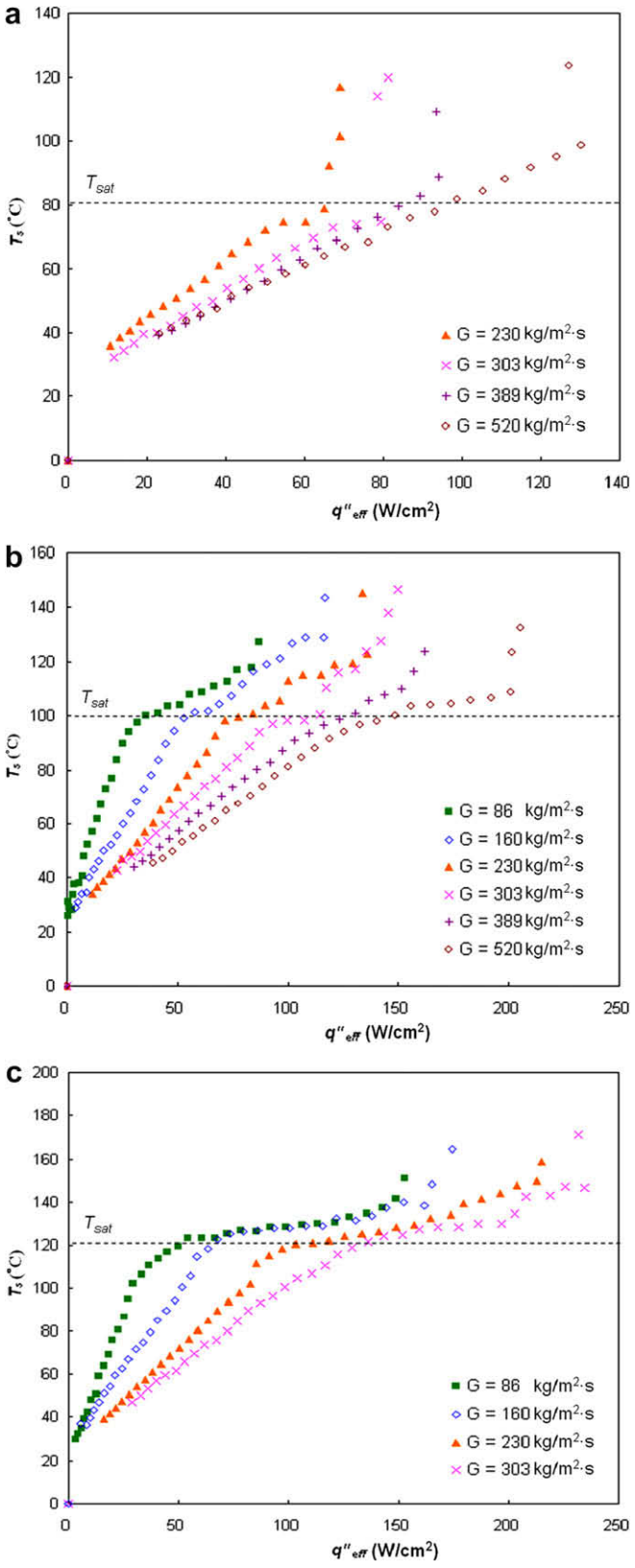

Fig. 5. Substrate temperature as a function of effective heat flux for (a) p = 50 kPa, (b) p = 101 kPa, and (c) p = 205 kPa.

that the ONB corresponded to this slope change. For p_e = 50 kPa, the boiling initiated with rapid bubble formation, resulting in rigorous flow oscillation, which lead to CHF condition immediately after ONB. This premature CHF is evident from the sharp increase of the

substrate temperature (Fig. 5a). On the other hand, for p_e = 101 kPa and 205 kPa, a stable boiling region was established after ONB, and was maintained until the heat flux reached a condition where boiling instability commenced with considerable temperature fluctuations. The onset of flow oscillation (OFO) was marked and defined as the conditions corresponding to a substrate temperature fluctuation greater than 5% of T_{sat} (in °C). As the heat flux further increased, so did the magnitude of the flow oscillation.

Flow boiling in channels is strongly affected by the mass flux (G), the mass quality (x), the channel exit pressure (p_e), the channel hydraulic diameter (d_h), the channel length (L_0), the number of (parallel) channels (N), and the fluid properties [26]. Therefore, onset of boiling instability of water in a given heat sink (i.e., fixed d_h, L_0, and N), can be expressed as:

$$q''_{OFO} = f(G, x_e, p_e) \tag{7}$$

where x_e is the exit mass quality.

Comparisons of the exit qualities at ONB, OFO, and CHF as a function of mass flux are depicted in Fig. 6. The corresponding exit qualities at OFO and CHF for p_e = 205 kPa are significantly higher than for p_e = 50 and 101 kPa. The exit qualities at ONB for p_e = 50 kPa are much higher than for the higher pressures and rigorous flow oscillation was initiate immediately after boiling inception. Although the exit qualities at OFO for p_e = 50 and 101 kPa are fairly similar, the magnitude of oscillation for p_e = 50 kPa following OFO was much larger than for p_e = 101 kPa. This significant larger magnitude of oscillation for p_e = 50 kPa resulted in very early transition to CHF (Fig. 6c). The reduced flow oscillations and the corresponding increase in CHF is very distinct for p_e = 205 kPa. There are several possible causes for this strong pressure effect. The system pressure can modify several important independent variables pertinent to flow boiling: the vapor density (ρ_v), the surface tension (σ), and the latent heat of vaporization (h_{lv}). For the pressure range of the current study, the surface tension and the latent heat of vaporization vary moderately (5–10%) with the saturation pressure (or temperature), but the vapor density varies by a factor of four. Therefore, the effects of σ and h_{lv} seem to be secondary in determining the dominant parameters controlling boiling instability. Eq. (7) can thus, be rewritten as:

$$q''_{OFO} = f(G, x_e, \rho_v) \tag{8}$$

For higher system pressures at a given mass quality, the diminishing liquid-to-vapor density ratio reduces the void fraction in the channel. Since *density wave* oscillations are closely related to the

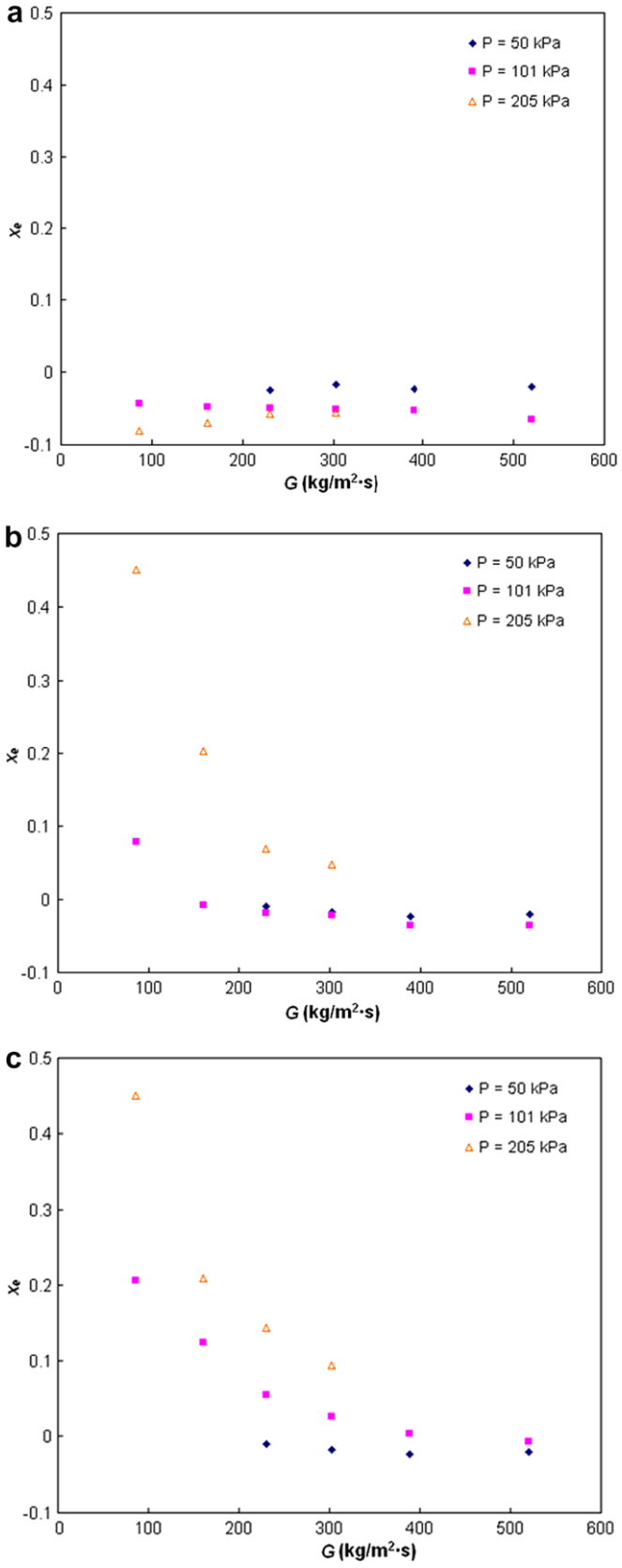

Fig. 6. Exit qualities at (a) ONB, (b) OFO, and (c) CHF for different mass fluxes at different system pressures.

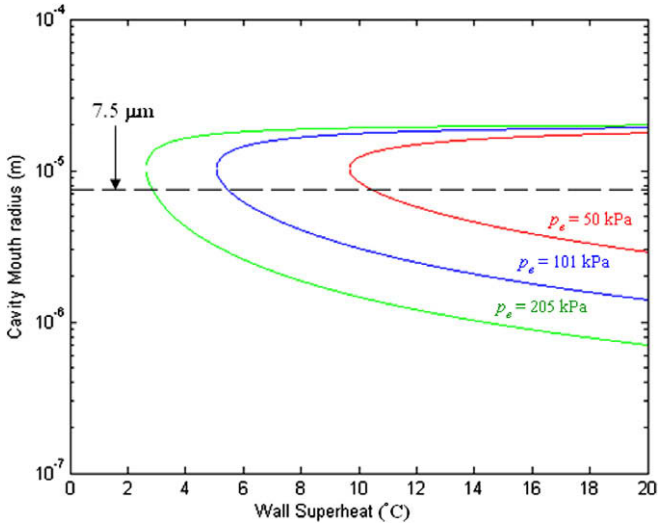

Fig. 7. Active mouth diameter as a function of wall superheat for different exit pressures based on Hsu's criteria [27].

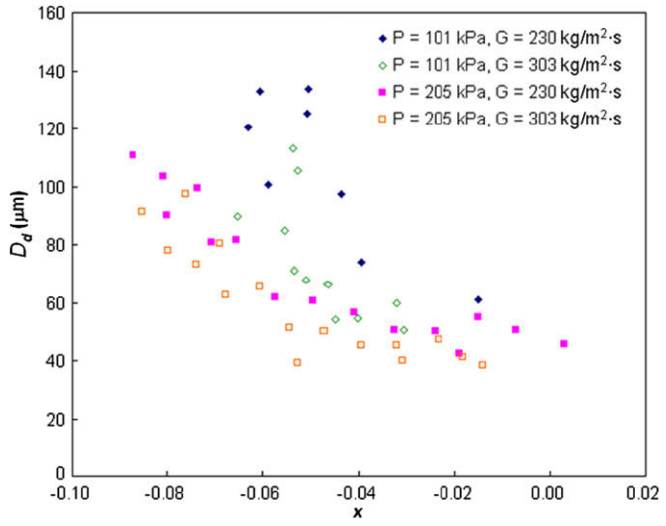

Fig. 8. Bubble departure diameter, D_d, as a function of local mass quality, x, for different pressure and mass flux.

void fraction response to disturbances, reduction of the void fraction stabilizes the flow. The decrease of void fraction reduces the two-phase flow friction and momentum pressure drop in the channel and extends the metastable boiling region (segment b–d in Fig. 1) to higher mass quality [6], which in turn delays the *excursive instability*. Reducing the void fraction in the channel also moderates the two-phase flow pressure drop - mass flux slope of the negative slope segment (modifying segment d–e to segment d–e′ in Fig. 1) and alleviates the tendency of *excursive/compressible volume instability* to be triggered.

Another instability that can be moderated at high system pressure is the *rapid bubble growth*. If the liquid superheat temperature is reduced, so does the violent explosive characteristic during the rapid bubble growth. This in turn prevents premature transition from the stable region (segment b–d in Fig. 1) to the unstable region of the pressure drop–mass flux curve (segment d–f in Fig. 1). The effect of pressure on the superheat temperature required for the onset of boiling can be evaluated using Hsu's model [27]:

$$\{D_{c,\max}, D_{c,\min}\} = \frac{\delta_t C_2}{2C_1}\frac{\Delta T_w}{\Delta T_w + \Delta T_{sub}} \times \left[1 \pm \sqrt{1 - \frac{8C_1\sigma T_{sat}(\Delta T_w + \Delta T_{sub})}{\rho_v h_{lv}\delta_t(\Delta T_w)^2}}\right] \quad (9)$$

where $D_{c,\max}$ and $D_{c,\min}$ are the maximum and minimum diameters of active nucleation sites, respectively. C_1 and C_2 are constants de-

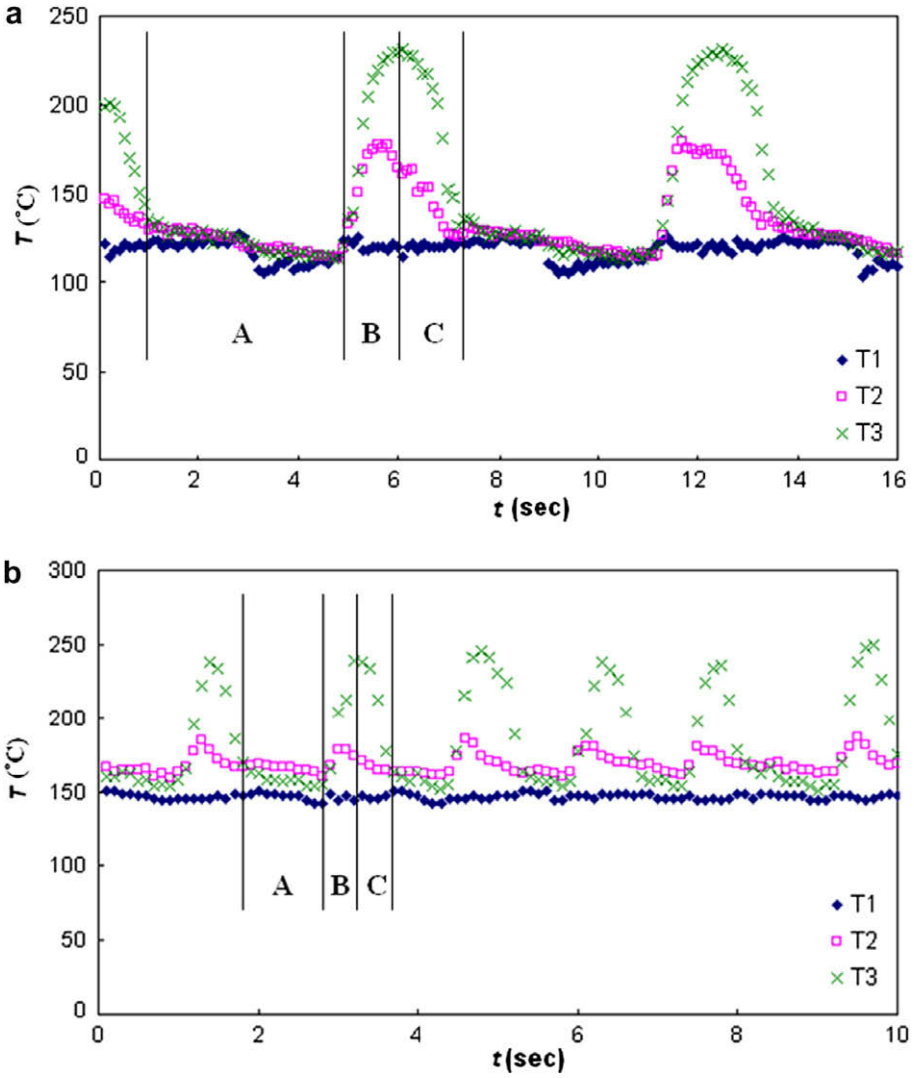

Fig. 9. Transient temperature at different locations in the microchannel for (a) p = 101 kPa, G = 303 kg/m^2 s, x_e = 0.02 and (b) p = 205 kPa, G = 303 kg/m^2 s, x_e = 0.08.

fined as: $C_1 = 1 + \cos\phi$, $C_2 = \sin\phi$. The wall superheat and bulk liquid subcooled temperature are $\Delta T_w = T_w - T_{sat}$ and $\Delta T_{sub} = T_{sat} - T_f$, respectively. Assuming linear temperature profile in the liquid boundary layer [28]:

$$\delta_t = \frac{k_l}{h_{sp}} \tag{10}$$

For $Nu = 5.5$ (thermal and hydraulic fully developed flow), $\delta_t \sim 40$ μm. Fig. 7 shows the size of active nucleation sites as a function of wall superheat for different exit pressures with contact angle $\phi = 57°$ and $\Delta T_{sub} = 0$ °C. The artificial reentrant cavity mouth diameter (7.5 μm) is also shown in the figure. The wall superheat required activating nucleation sites decreases with increasing exit pressure, and a wider range of nucleation site is activated. As discussed earlier and in Kuo and Peles [24], it follows that the rapid bubble growth, and consequently the premature transition to excursive instability, is suppressed with increasing pressure.

The effect of the violent growth of a vapor bubble on the global flow field in a channel is also related to the bubble departure diameter (D_d). Smaller bubbles tend to result in lower magnitude of flow oscillations, and their effect on the main flow is less significant. Bubble departure diameter was obtained from the high speed images captured during the visualization study. Fig. 8 shows the bubble departure diameter as a function of local mass quality (x) for different system pressures for $G = 230$ kg/m^2 s and $G = 303$ kg/m^2 s. The results of the present study concur with conventional scale results, which suggest that the bubble departure diameter diminishes with increasing pressure [29–39]. The diminishing bubble departure diameter can be a result of the reduced wall superheat required for bubble nucleation, as discuss above, or a result of increasing vapor density. The results shown in Fig. 8 provide some quantitative visualization evidence that the bubble growth process affects the global flow (and pressure) field more significantly at lower pressures. It also supports the argument discussed earlier that at low pressures the *rapid bubble growth instability* elevates and its high magnitude of oscillation causes premature transition to the negative slope segment of the pressure–mass flow rate curve (*excursive instability*). Without inlet restrictors [17], a transition to the unstable region (segment d–f in Fig. 1) results in rapid and possibly immediate transition to premature CHF condition upon boiling inception. For higher pressures ($p_e = 205$ kPa), the low superheat temperature during the phase change process moderates the *rapid bubble growth* and eliminates early boiling instability. It also forms a gradual and well-distributed boiling process, which reduces the flow oscillation and enhances the CHF.

4.2. Transient thermal–hydraulic characteristic

Fig. 9 shows the local transient temperature at different locations in the microchannel for $p_e = 101$ kPa, $G = 303$ kg/m^2 s,

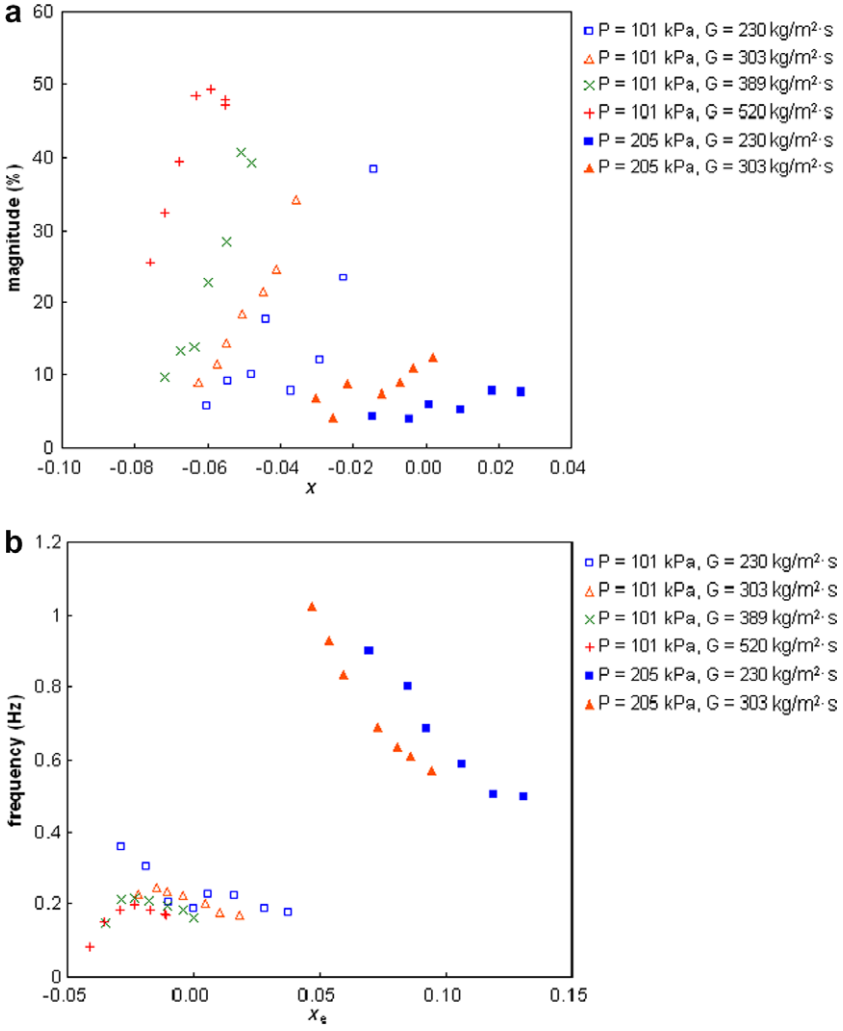

Fig. 10. (a) Magnitude of flow oscillation as a function of local mass quality. (b) Frequency of flow oscillation as a function of exit mass quality.

$x_e = 0.02$ (Fig. 9a) and $p_e = 205$ kPa, $G = 303$ kg/m^2 s, $x_e = 0.08$ (Fig. 9b). As discussed by Kuo and Peles [24], for unstable boiling in microchannels at atmospheric pressure, the characteristic thermal–hydraulic cycle can be divided into three distinct stages: bubble nucleation (stage A), vapor filling/dryout (stage B), and post dryout/upstream flooding (stage C). Local transient temperature measurements showed a similar cycle for $p_e = 205$ kPa (Fig. 9b). However, a relatively stable upstream temperature (T_1 and T_2) was observed, which is believed to be caused by the suppression of the *rapid bubble growth* and the more consistent bubble generation at $p_e = 205$ kPa. As a result, the tendency of the flow to propagate upstream is alleviated and stable thermal–hydraulic conditions are more likely to exist.

To further evaluate the nature of flow boiling instabilities for $p_e = 101$ and 205 kPa, the magnitudes and frequencies of T_2 oscillations are shown in Fig. 10 as a function of mass quality for different mass fluxes. Much smaller oscillation magnitudes were observed for $p_e = 205$ kPa than for $p_e = 101$ kPa. For the same hydraulic condition, the magnitude of oscillation increases with mass quality, as a direct result of the increased void fraction. Frequencies from 0.4 to 1 Hz for $p_e = 205$ kPa and 0.1–0.4 Hz for $p_e = 101$ kPa were observed – at the macro-scale, typical frequency of *pressure drop instability* is ~0.1 Hz and of *density wave instability* is ~1 Hz. As the mass quality/heat flux increases in the microchannel, a longer time period is needed to dissipate the heat during the transient cycle, which results in reduced frequency of oscillation. This is especially significant for $p_e = 205$ kPa. Pressure drop oscillation is a compound phenomenon of static instability (flow excursion) and dynamic instability (density wave) [6]. For conventional scale system, *pressure drop/compressible volume instability* often encounters or combines with *density wave instability*. While *pressure drop instability* frequently results in large oscillation magnitudes of flow rate, pressure drop, and wall temperature, Saha et al. [40] argued that *density wave instability* does not trigger appreciable magnitude of wall temperature oscillation in the two-phase region. The small magnitudes and higher frequencies of oscillation for $p_e = 205$ kPa suggest that boiling instability mechanism for the higher pressure is *density wave instability* rather than *pressure drop instability*. Additionally, it is suggested by Stenning et al. [41] that for low mass flow rates, *density wave instability* (high frequency), and not *pressure drop instability* (low frequency), prevails. This is also observed in the current microchannels as higher frequency was more notable at low mass fluxes for both system pressures (Fig. 10b).

5. Conclusion

The current paper reports on pressure effect on flow boiling instabilities in microchannels. Various boiling instability modes previously identified in macro- and microchannels (i.e., *excursive*, *compressible volume*, *rapid bubble growth*, and *density wave instabilities*) were examined. OFO, CHF condition, bubble departure diameter, and local temperature measurements at different pressures were acquired and compared. The main conclusions drawn from the study are:

1. The increase of system pressure at a given mass quality reduces the void fraction and the momentum pressure drop across the channel. This in turn, contains and delays the *excursive/compressible volume instability*.
2. For high pressure, the low superheat needed to activate bubble nucleation during flow boiling inhibits rapid bubble growth instability and prevents hasty transition to CHF condition.
3. Flow visualization revealed smaller bubble departure diameters at high system pressure. The reduction of bubble departure diameter is an indicative of reduced rapid bubble growth oscillation.
4. Local transient temperature measurements showed lower magnitudes and higher frequencies of oscillations at high system pressure. The higher frequencies may be linked to *density wave instability* and can result in low temperature oscillation magnitude.

Acknowledgements

This work was supported by the Office of Naval Research (ONR) through the Young Investigator Program under Contract No. N00014-05-1-0582. The micro-device was fabricated in Cornell Nanofabrication Facility (CNF), a member of the national nanotechnology Infrastructure Network, which is supported by the National Science Foundation (NSF) under Grant No. ECS-0335765, its user, Cornell University, and the industrial affiliates. The authors extend their gratitude to the staff and students on the CNF.

References

[1] L. Zhang, J. Koo, L. Jiang, M. Asheghi, K.E. Goodson, J.G. Santiago, T.W. Kenny, Measurements and modeling of two-phase flow in microchannels with nearly constant heat flux boundary conditions, IEEE JMEMS 11 (1) (2002) 12–19.
[2] S.G. Kandlikar, Heat transfer mechanism during flow boiling in microchannels, J. Heat Transfer 126 (2004) 8–16.
[3] J.R. Thome, Boiling in microchannels: a review of experiment and theory, Int. J. Heat Fluid Flow 25 (2004) 128–139.
[4] T. Chen, S.V. Garimella, Measurements and high-speed visualizations of flow boiling of a dielectric fluid in a silicon microchannel heat sink, Int. J. Multiphase Flow 32 (8) (2006) 957–971.
[5] S. Hardt, B. Schilder, D. Tiemann, G. Kolb, V. Hessel, P. Stephan, Analysis of flow patterns emerging during evaporation in parallel microchannels, Int. J. Heat Mass Transfer 50 (1–2) (2007) 226–239.
[6] J.A. Boure, A.E. Bergles, L.S. Tong, Review of two-phase flow instability, Nucl. Eng. Des. 25 (1973) 165–192.
[7] A.E. Bergles, S.G. Kandlikar, On the nature of critical heat flux in microchannels, J. Heat Transfer 127 (10) (2005) 101–107.
[8] M.B. Bower, I. Mudawar, High flux boiling in low flow rate, low pressure drop mini-channel and micro-channel heat sinks, Int. J. Heat Mass Transfer 37 (1994) 321–332.
[9] L. Jiang, M. Wong, Y. Zohar, Phase change in microchannel heat sinks with integrated temperature sensors, IEEE JMEMS 8 (1999) 358–365.
[10] S. Mukherjee, I. Mudawar, Smart, low-cost, pumpless loop for micro-channel electronic cooling using flat and enhanced surface, in: Proc. JTherm 2002, IEEE, Piscataway, NJ, pp. 360–370.
[11] W. Qu, I. Mudawar, Measurement and correlation of critical heat flux in two-phase micro-channel heat sinks, Int. J. Heat Mass Transfer 47 (2004) 2045–2059.
[12] J.E. Kennedy, G.M. Roach Jr., M.F. Dowling, S.I. Abdel-Khalik, S.M. Ghiaasiaan, S.M. Jeter, Z.H. Quershi, The onset of flow instability in uniform heated horizontal microchannels, J. Heat Transfer 122 (2000) 118–125.
[13] H.Y. Wu, P. Cheng, Visualization and measurements of periodic boiling in silicon microchannels, Int. J. Heat Mass Transfer 46 (2003) 2603–2614.
[14] K.H. Chang, C. Pan, Two-phase flow instability for boiling in a microchannel heat sink, Int. J. Heat Mass Transfer 50 (11–12) (2007) 2078–2088.
[15] T.-H. Yen, M. Shoji, F. Takemura, Y. Suzuki, N. Kasagi, Visualization of convective boiling heat transfer in single microchannels with different shaped cross-sections, Int. J. Heat Mass Transfer 49 (21–22) (2006) 3884–3894.
[16] L. Tadrist, Review on two-phase flow instability in narrow spaces, Int. J. Heat Fluid Flow 28 (1) (2007) 54–62.
[17] A. Koşar, C.-J. Kuo, Y. Peles, Suppression of boiling flow oscillations in parallel microchannels with inlet restrictors, J. Heat Transfer 128 (3) (2006) 251–260.
[18] S.G. Kandlikar, W.K. Kuan, D.A. Willistein, J. Borrelli, Stabilization of flow boiling in microchannels using pressure drop elements and fabricated nucleation sites, J. Heat Transfer 128 (4) (2006) 389–396.
[19] G. Wang, P. Cheng, A.E. Bergles, Effects of inlet/outlet configurations on flow boiling instability in parallel microchannels, Int. J. Heat Mass Transfer 51 (9–10) (2008) 2267–2281.
[20] A. Koşar, C.-J. Kuo, Y. Peles, Boiling heat transfer in rectangular microchannels with reentrant cavities, Int. J. Heat Mass Transfer 48 (23–24) (2005) 4867–4886.
[21] C.-J. Kuo, A. Koşar, Y. Peles, S. Virost, C. Mishra, M.K. Jensen, Bubble dynamics during boiling in enhanced surface microchannels, IEEE JMEMS 15 (6) (2006) 1514–1527.
[22] C.-J. Kuo, Y. Peles, Local measurement of flow boiling in structured surface microchannels, Int. J. Heat Mass Transfer 50 (23–24) (2007) 4513–4526.
[23] R.J. Jones, D.T. Pate, S.H. Bhavnani, Control of instabilities in two-phase microchannel flow using artificial nucleation sites, in: Proceedings of the IPACK 2007, ASME InterPack'07, IPACK2007-33602.

[24] C.-J. Kuo, Y. Peles, Flow boiling instabilities in microchannels and means for mitigation by reentrant cavities, J. Heat Transfer 130 (7) (2008).
[25] S. Kline, F.A. McClintock, Describing uncertainties in single-sample experiments, Mech. Eng. 75 (1) (1953) 3–8.
[26] J.G. Collier, J.R. Thome, Convective Boiling and Condensation, third ed., Oxford University Press, Oxford, 1994. pp. 193–195.
[27] Y.Y. Hsu, On the size range of active nucleation cavities on a heating surface, J. Heat Transfer 84 (1962) 207–216.
[28] V.P. Carey, Liquid–Vapor Phase-Change Phenomena, Taylor & Francis, London, 1992. pp. 565–571.
[29] W. Fritz, Berechnung des Maximalvolume von Dampfblasen, Phys. Z. 36 (1935) 379–388.
[30] N. Zuber, Hydrodynamic aspects of boiling heat transfer, US AEC report AECU 4439, June, 1959.
[31] E. Ruckenstein, Physical model for nucleate boiling heat transfer from a horizontal surface, Appl. Mech. Rev. 16 (1963). Rev. 6055.
[32] R. Cole, H.L. Shulman, Bubble departure diameter at subatmospheric pressure, Chem. Eng. Prog. Symp. Ser. 62 (64) (1966) 6–16.
[33] R. Cole, Bubble frequencies and departure volumes at subatmospheric pressure, AICHE J. 13 (1967) 779–783.
[34] S.S. Kutateladze, I.I. Gogonin, Growth rate and detachment diameter of a vapor bubble in free convection boiling of a saturated liquid, High Temp. 17 (1979) 667–671.
[35] V.M. Borishanskiy, G.N. Danilova, M.A. Gotovskiy, A.V. Borishanskiy, G.P. Danilova, A.V. Kupriyanova, Correlation of data on heat transfer in, and elementary characteristics of the nucleate boiling mechanism, Heat Transfer Sov. Res. 13 (1) (1981) 100–116.
[36] G. Kocamustafaogullari, Pressure dependence of bubble departure diameter for water, Int. Commun. Heat Mass Transfer 10 (1983) 501–509.
[37] M.K. Jensen, G.J. Memmel, Evaluation of bubble departure diameter correlations, in: Proceedings of the Eighth International Heat Transfer Conference, vol. 4, 1986, pp. 1907–1912.
[38] C.-P. Yin, Y.-Y. Yan, T.-F. Lin, B.-C. Yang, Subcooled flow boiling heat transfer of R-134a and bubble characteristics in a horizontal annular duct, Int. J. Heat Mass Transfer 43 (11) (2000) 1885–1896.
[39] Y.M. Lie, T.F. Lin, Subcooled flow boiling heat transfer and associated bubble characteristics of R-134a in a narrow annular duct, Int. J. Heat Mass Transfer 49 (13–14) (2006) 2077–2089.
[40] P. Saha, M. Ishii, N. Zuber, An experimental investigation of the thermally induced flow oscillations in two-phase systems, J. Heat Transfer 98 (1976) 616–622.
[41] A.H. Stenning, T.N. Veziroglu, G.M. Callahan, Pressure-drop oscillations in forced convection flow with boiling, EURATON Report, in: Proceedings of the Symposium on Two-Phase Flow Dynamics, EUR 4288e, 1967, pp. 405–427.